Electronic Supplementary Information (ESI)

Ultrasound defect sensitive blue-shifted emissive mechanochromic material for detection of Cu^{2+} in Alzheimer disease cells

Aayoosh Singh[a], Pranjalee Yadav[a], Amit K. Singh[a], Rupen Tamang[b], Biplob Koch[b], and Vinod P. Singh[a,†]

[a]*Department of Chemistry, Institute of Science, Banaras Hindu University, Varanasi-221005, India*

[b]*Department of Zoology*, *Banaras Hindu University, Varanasi-221005, India*

Table of Contents

Experimental methods, measurements and calculations

Instrumentation

KBr pellets were used to record FT-IR spectra in the 4000-400 cm^{-1} region on a FT-IR 4700 JASCO spectrophotometer. The JEOL Resonance Inc. multinuclear FT NMR spectrometer (Model-ECZ-500R) was used to obtain ^1H and ^{13}C NMR spectra in DMSO-d_6. The chemical shifts are given in parts per million (ppm) with respect to an internal standard of tetramethylsilane (TMS) at room temperature. ESI-mass spectra were recorded on a HRMS SCIEX X-500R QTOF spectrometer. The Shimadzu UV-1800 spectrophotometer was used to record all the UV-Vis. spectra. Fluorescence spectra were obtained using a Fluromax 4CP plus fluorescence spectrophotometer (slit = 5 nm). The LMPH-10 pH meter was used to monitor and adjust the pH of various solutions. Melting points were measured using a digital melting point apparatus at a heating rate of 10 ^oC/min. The EVO-Scanning Electron Microscope MA15/18 (Carl ZEISS Microscopy Ltd.) was used to capture the SEM images. TEM images were captured with TECNAI 20G2 200KV (Thermo Fischer Company). WITec alpha300 RAS (made in Germany) with a 405 nm pulsed diode laser was used to record TRPL. DLS measurements were conducted on a Zetasizer Ultra (ZSU5700) Particle Size Analyzer, Malvern Panalytical (UK). A Bruker D8 Advance powder X-ray diffractometer equipped with Cu Kα radiation with a LyneEye detector was used for the powder X-ray diffraction experiments. Solid state fluorescence was recorded on a Fluorolog FL-3C-21 UV-Vis-NIR-Spectrofluorometer with an integrated sphere (steady-state). Thermal property was analysed by differential scanning calorimetry (DSC) on a Mettler Toledo Model-822e instrument in nitrogen environment at the heating rate of 10 ^oC/min.

X-ray crystallography

The Rigaku XtaLAB Synergy-I diffractometer with CrysAlisPro was used to conduct the single crystal X-ray diffraction studies with a graphite monochromated Cu Kα (λ = 1.54184) radiation source. Measurements were taken for the probe and metal complex at ambient temperature. The structure was solved with SHELXL-97 and optimised with full matrix least-

squares on F^2 and anisotropic displacement parameters for all non-hydrogen atoms.[1,2] All hydrogen atoms were refined into their geometrically ideal positions using a riding model. The structure was generated using the MERCURY programme and the ORTEP-3 Windows application.[3] **Table S1** summarises the crystal data and structure determination information for **CFH** and **CFH**-Cu^{2+}.

Reagents and materials

Piperidine, ethyl acetoacetate, 4-(diethylamino)-2-hydroxybenzaldehyde, and furan-2-carbohydrazide were obtained from Sigma-Aldrich Chemicals, USA, and were used without further purification. Solvents, reagents and metal salts were all of analytical grade. Millipore water was used in all experiments. The National Centre for Cell Science, Pune, India, provided the SH-SY5Y and HEK-293 cell lines for bio-imaging analysis. DMEM, FBS, Trypsin-EDTA, and antibiotics (Penicillin-Streptomycin) were procured from Cell Clone. 96-well plates were supplied from Eppendorf and 12-wells from Genetix.

Structural characterization of CFH

The IR spectral bands appearing at 3110, 1719, 1683 and 1604 cm^{-1} are assigned to ν(NH), $\nu(C{=}O)_{\text{lactone ring}}$, $\nu(C{=}O)_{\text{amide}}$ and ν(C=N), respectively (ESI, Fig. S1†). The ^{1}H-NMR signal for –NH proton occurs at 10.47 ppm. The signals observed in the region 8.02–6.50 ppm are attributed to the aromatic ring protons. The signal observed at 3.39 ppm is due to $>CH_2$ protons and the signals at 2.24 and 1.08 ppm are for $–CH_3$ groups attached to >C=N and $>CH_2$ groups, respectively (ESI, Fig. S2†). In ^{13}C-NMR spectrum, signals for $>(C{=}O)_{\text{amide}}$, $>(C{=}O)_{\text{lactone ring}}$ and >C=N groups are observed at 160.54, 157.08 and 151.68 ppm, respectively. Furthermore, $>CH_2$ carbons appears at 44.70 ppm and signals at 16.60 and 12.87 ppm correspond to methyl carbons attached to >C=N and $>CH_2$ groups, respectively (ESI, Fig. S3†). The signals observed in the range of 146.40–96.65 are due to aromatic carbons. In HRMS spectrum of **CFH**, the molecular ion peak observed at m/z= 368.1709 correlates well to $[M + H]^+$ and validates the molecular formula (ESI, Fig. S4†)

Fluorescence and UV-Vis measurements

CFH (1 mM) stock solution was prepared at room temperature in DMSO. Metal ion solutions (1 mM) were made in Milli-Q water using their nitrate, chloride, or acetate salts. To keep the concentration at 1 μM, the required volume of water (3 mL) were added to 3 μL of **CFH** solution for standard detection. The UV-Vis and fluorescence spectrophotometric titrations were done directly with a microliter pipette by adding the chemical reagents one at a time. The solution

was well mixed after each addition of aliquot before taking the spectra. Aggregation-induced enhanced emission (AIEE) property of **CFH** was studied at 1 μM concentration in THF solution with varying water fractions (f_w) from 0 to 99.9% (v/v). The viscochromic property of **CFH** was studied in EtOH solution at the concentration of 1 μM with varying fractions of glycerol (f_g) ranging from 0 to 99.9% (v/v).

Particle size determination using the DLS technique

DLS measurements for **CFH** in various fraction of THF:water (f_w 0 %, 50 %, and 99.9 %), including 1.0 equivalent of Cu^{2+} ions (at f_w=99.9%) were taken at 1 μM concentration.

TEM analysis

To do the TEM analysis, the drop casting method was used. 1 μM of **CFH** was mixed with THF-water solution at three different water fractions (f_w = 0%, 50%, and 99.9%) as well as **CFH** with 1 equivalent of Cu^{2+} ions at the 99.9% (f_w).

SEM analysis

The SEM measurements were carried out by drop casting of **CFH** (1 μM) dissolved in THF on cover slip and coating it with silver.

^{1}H NMR titration experiments

A 0.01 M solution of **CFH** was prepared in DMSO-d_6. Various equivalents of $Cu(NO_3)_2$ (from a stock of 0.1 M in DMSO-d_6) were added to 0.5 mL of **CFH** solution in NMR tube using a micro pipette and the spectra were recorded.

Preparation of test kit for determination of Cu^{2+}

Cotton earbuds with plastic handles and filter paper (Whatman, diameter = 125 mm) were used to prepare test kits to detect Cu^{2+} in real samples. Earbuds were made up of two parts: cotton (the sample area) and plastic (the holding area). For filter paper, the sample area was on the surface of the filter paper. A stock solution of **CFH** was prepared in DMF and diluted with Milli-Q water to achieve a concentration of 1 μM. Earbuds and filter paper were submerged in the prepared stock solution for 10 min before drying in the air. The dried earbud test kits are now ready to detect Cu^{2+} in a pool of metal ions. Dried filter paper was cut into 20 mm discs for further investigation.

Cell viability evaluation

To evaluate the biocompatibility of the probe **CFH**, MTT assay was performed on the SH-SY5Y and HEK-293 cell lines. The SH-SY5Y cell line was used as a neurodegenerative disorder cell model, while HEK-293 was used as normal cells. The above SH-SY5Y and HEK-293 cell lines were trypsinized and seeded in 96-well plates at the density of 1×10^4 cells per well. The cells were then incubated for 24 h at 37 ºC in a CO_2 incubator. After incubation, the cells were treated with variable concentrations ranging from 1 μM to 30 μM of probe **CFH** for 24 h. The spent media was discarded, and MTT solution (100 μL) was added to each well, followed by a further 2 h of incubation. Sequentially, DMSO was applied to each well to dissolve the formazan crystals that had formed after removing the media, followed by a 30 min incubation period. Subsequently, the absorbance of each well was measured using a microplate reader at 570 nm.

Intracellular uptake

The properties of probe **CFH** were further explored in SH-SY5Y and HEK-293 cell lines through a bioimaging technique. The cells (HEK-293/ SH-SY5Y) were seeded at the required density after the trypsinization in 12 well plates and incubated overnight for adherence to the substratum. The process further proceeded with the probe treatment at the different concentrations (1-30 μM) for 24 h. After the completion of 24 h incubation of cells with a probe, the bioimaging analysis was done utilizing an inverted fluorescent microscope (Life Technologies, EVOS live cell imaging equipment). Additionally, HEK-293 cells were also seeded and given the same treatment however prior to 1 h of bioimaging, the cells were treated with Cu^{2+} treatment.

Quantum yield calculations

Quantum yield was determined by applying the following equation:[4]

$$Q = Q_r(I/I_r)(OD_r/OD)(n^2/n_r^2)$$

Where, Q, I, OD and n are fluorescence quantum yield, integrated fluorescence intensity, the refractive index of liquid and optical density (absorption), respectively. Subscript r represents the known quantum yield of reference quinine sulphate in 0.1 M H_2SO_4.

Fluorescence decay calculations

Time-resolved fluorescence lifetime experiments of **CFH** for AIEE, sensing properties and viscochromism have been performed at 1 μM concentration. The dynamic parameters and weighted mean lifetime <τ> were computed using the following equations:

$$y = A_1 * \exp\left(-\frac{x}{\tau_1}\right) + A_2 * exp\left(-\frac{x}{\tau_2}\right) + y_0$$

$$<\tau> = (A_1\tau_1 + A_2\tau_2)/(A_1 + A_2)$$

Where, τ_1/τ_2 and A_1/A_2 are the fractions or lifetimes (τ) and amplitudes (A), respectively.

The following equations are used to compute the radiative rate constant (K_r) and non-radiative rate constant (K_{nr}):[5]

$$<\tau^{-1}> = (K_r + K_{nr})$$

$$K_r = \frac{\Phi}{<\tau>}$$

Stern–Volmer constant (K_{SV}) calculation

The extent of fluorescence quenching was calculated using the Stern-Volmer equation:[8]

$$I_0/I = 1 + K_{sv}[Cu^{2+}]$$

Where, K_{SV} represents the Stern–Volmer quenching constant, and I_0 and I respectively indicate the fluorescence intensities with or without the presence of Cu^{2+} ions at various concentrations.

Calculation of binding constant and limit of detection (LOD)

The 1:1 binding ratio of **CFH** for Cu^{2+} was calculated using Job's plot and the binding constants (K_a) of **CFH** for Cu^{2+} were determined using the Benesi-Hildebrand equation:[6]

$$\frac{I_0}{I - I_0} = \frac{a}{b - a}\left(\frac{1}{K_a[Cu^{2+}]} + 1\right)$$

where, a and b are constants, I and I_0 are fluorescence intensities of **CFH** with and without Cu^{2+}; $[Cu^{2+}]$ is respective concentration of Cu^{2+} at 515 nm.

According to the IUPAC definition, the limit of detection (LOD) for **CFH** was determined using fluorescence titration data plotted against increasing Cu^{2+} concentration. The detection limit was calculated using the following equation:[7]

$$\text{LOD} = \frac{3SD}{Slope(m)}$$

Here, the standard deviation of blank observations is denoted by SD, and m is the slope of intensity

Computational details

DFT calculations were performed to validate the lowest-energy spatial conformation of **CFH**. Geometry optimizations were performed using the Gaussian 09 program. The 6-311++g(d,p) basis set and the B3LYP/LANL2DZ exchange-correlation functional were used.[9,10]

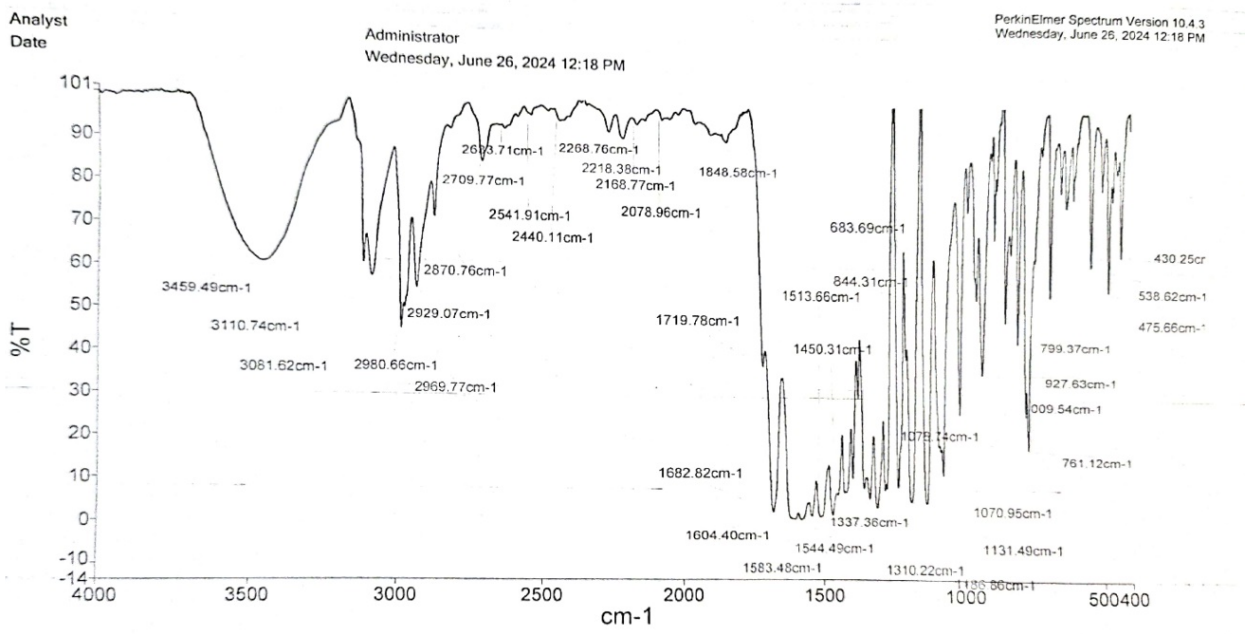

Fig. S1 IR spectrum of **CFH**

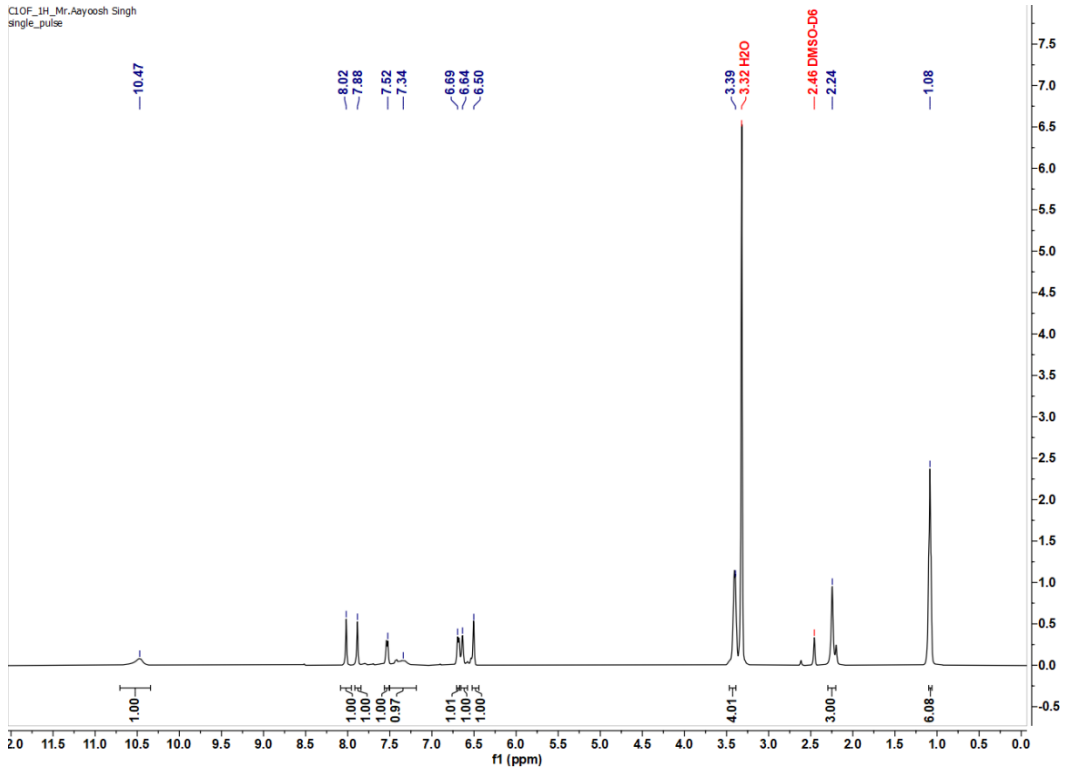

Fig. S2 ^{1}H-NMR spectrum of **CFH**

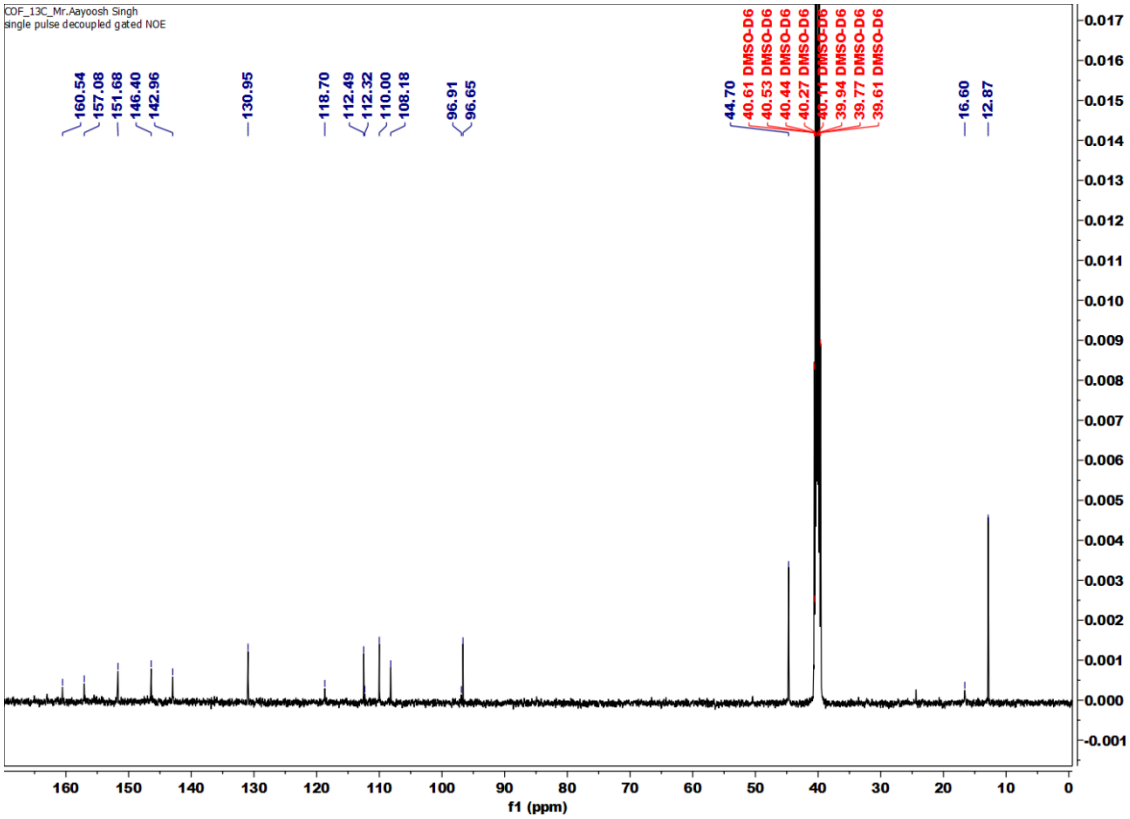

Fig. S3 ^{13}C-NMR spectrum of **CFH**

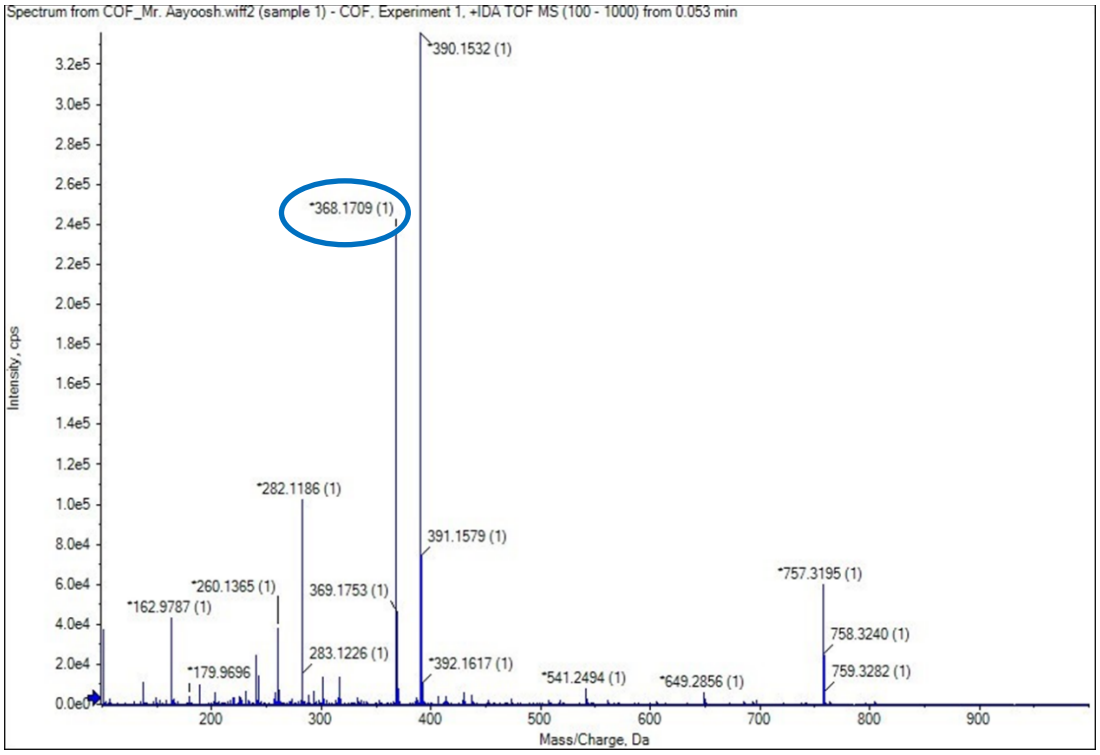

Fig. S4 HRMS spectrum of **CFH**

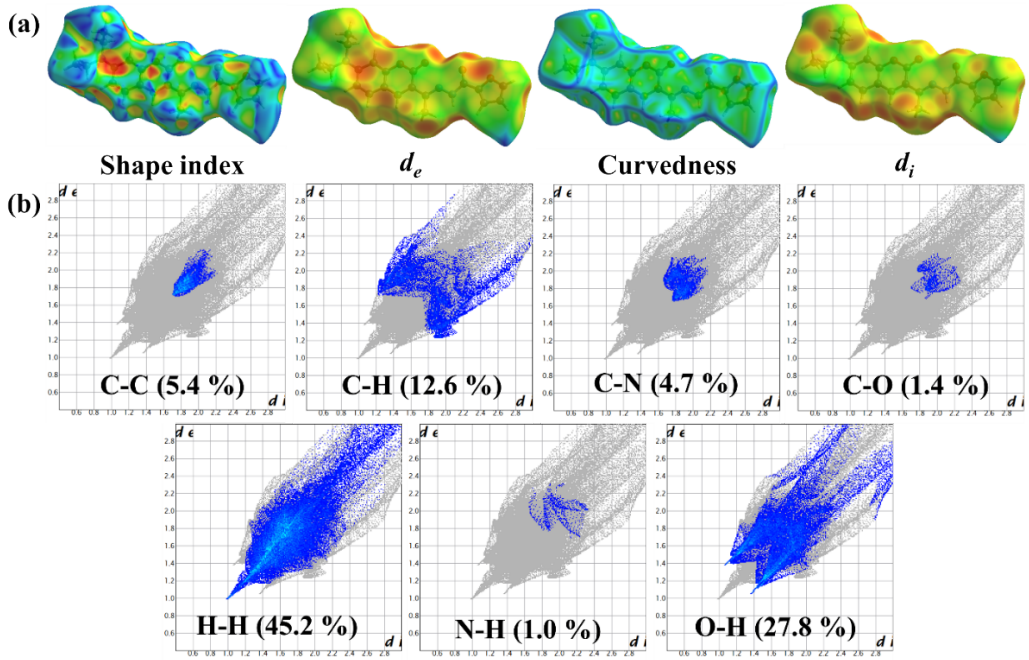

Fig. S5 (a) Hirshfeld surface analysis mapped over Shape index, d_e, curvedness and d_i, **(b)** 2D fingerprint plot of **CFH** displaying percentage of C-C, C-H, C-N, C-O, H-H, N-H and O-H interactions.

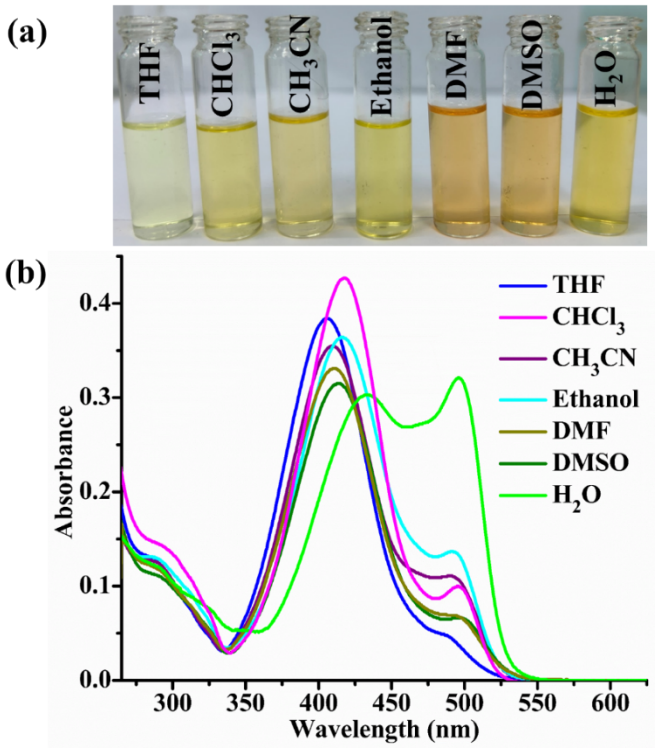

Fig. S6 (a) Photograph of **CFH** under natural light in solvents of different polarities**, (b)** UV-vis absorption spectrum of **CFH** (1 μM) in solvent of different polarities.

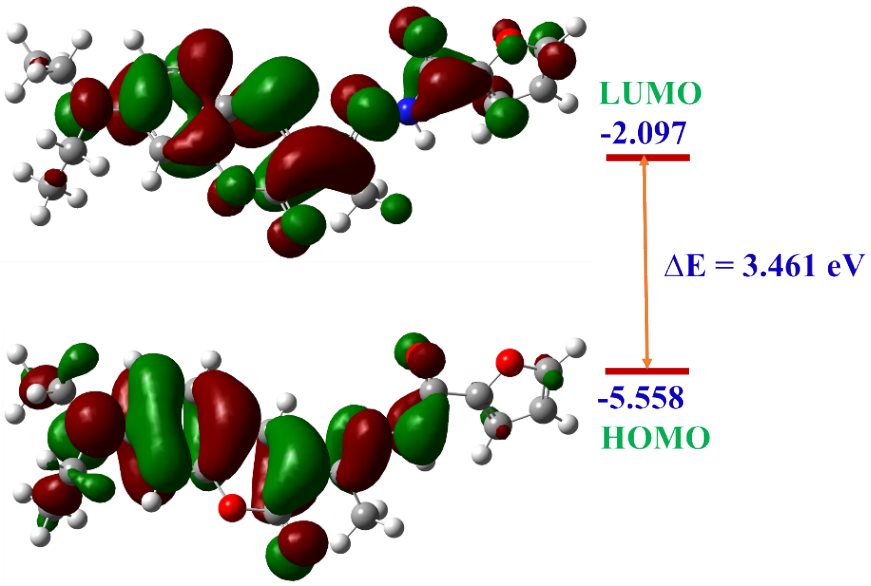

Fig. S7 DFT optimized structure of **CFH**

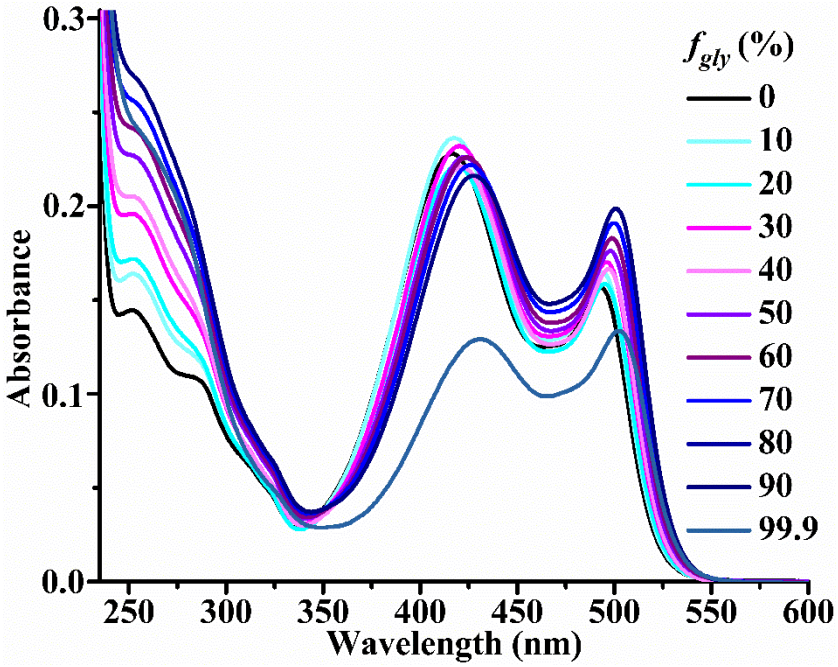

Fig. S8 UV-Vis absorption spectra of **CFH** (1 μM) at different glycerol fraction (f_{gly}) in ethanol.

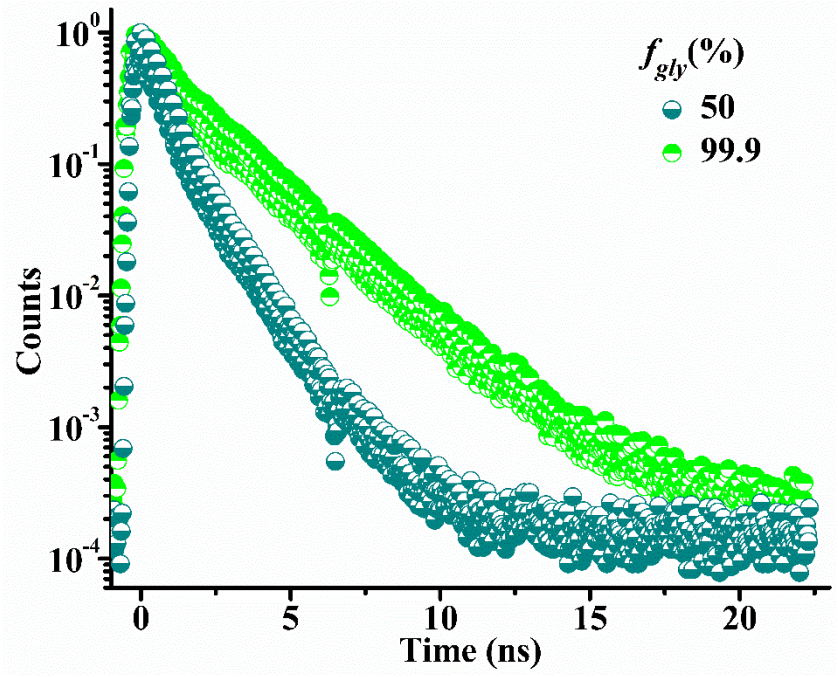

Fig. S9 Fluorescence lifetime spectra of **CFH** (1 μM) at varying glycerol fraction (f_{gly}) in ethanol.

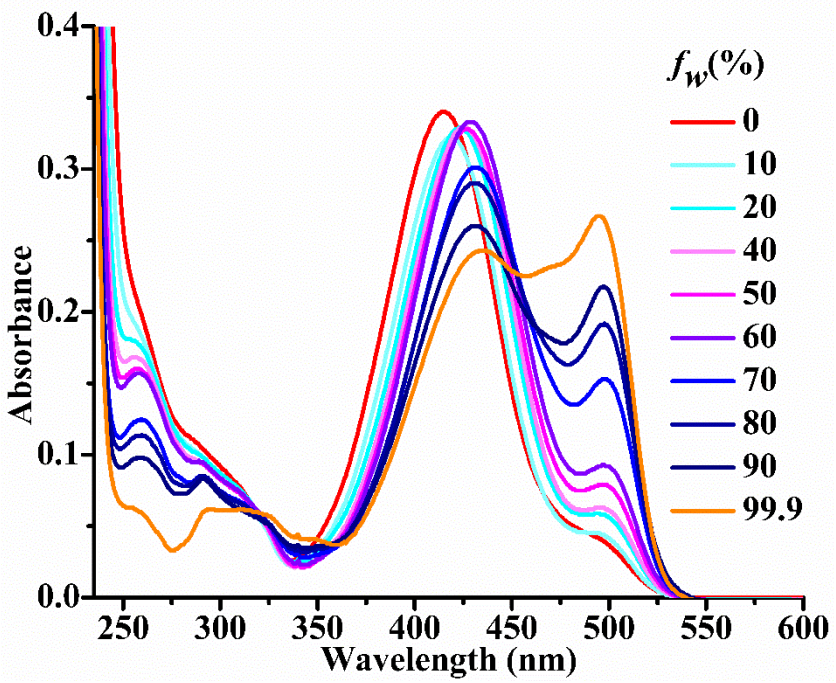

Fig. S10 UV-Vis absorption spectra of **CFH** (1 μM) at different water fraction (f_w) in THF.

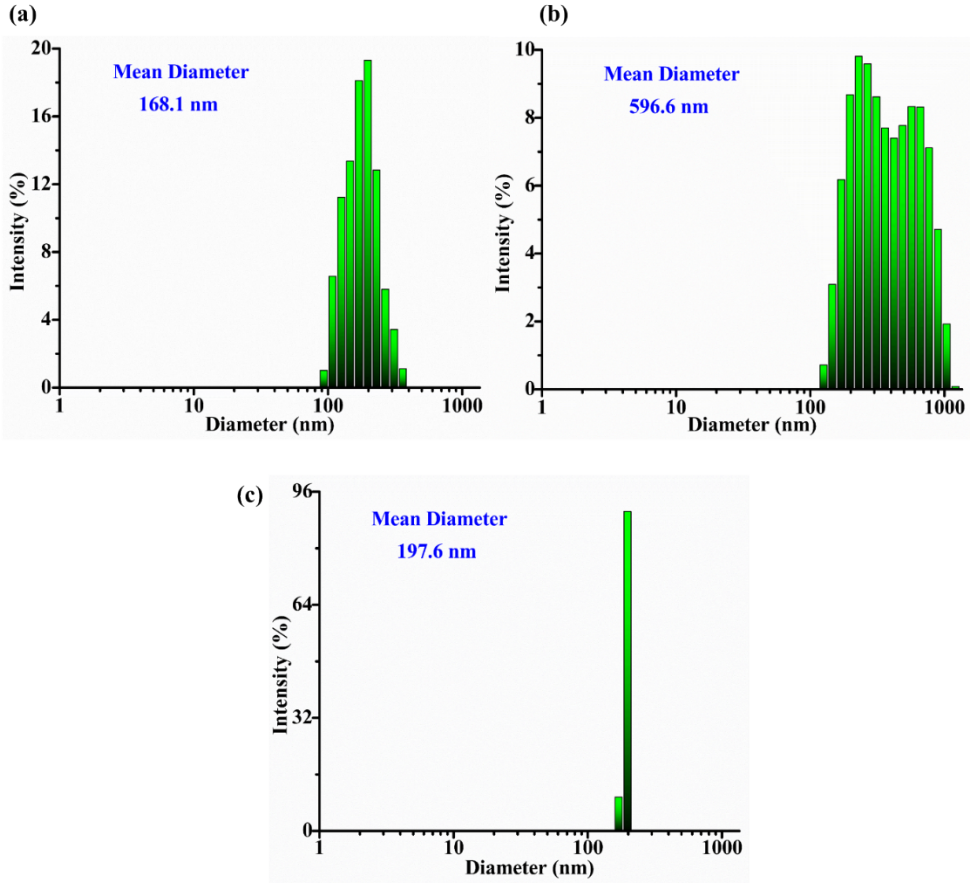

Fig. S11 Particle size measurements by DLS for **CFH** (1μM) at different water fraction (f_w) in THF, **(a)** f_w=0%, **(b)** f_w=50.0%, **(c)** f_w=99.9%.

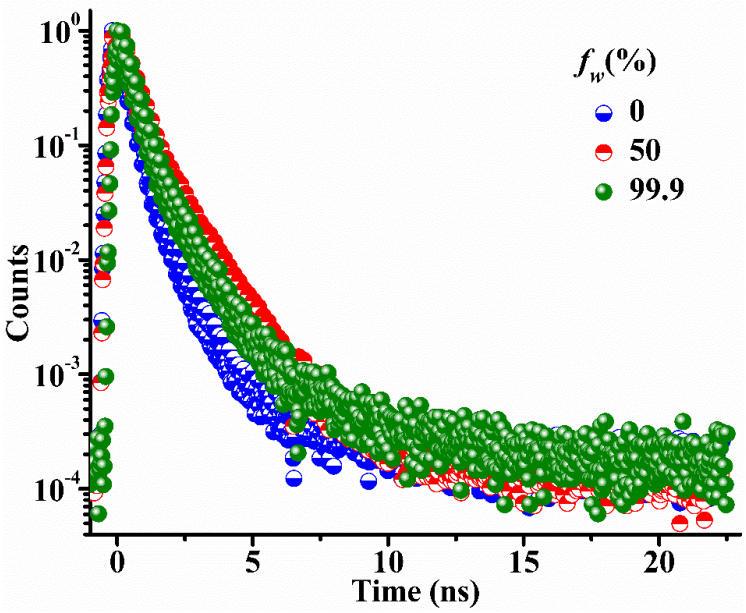

Fig. S12 Fluorescence lifetime spectra of **CFH** (1μM) at different water fraction (f_w) in THF.

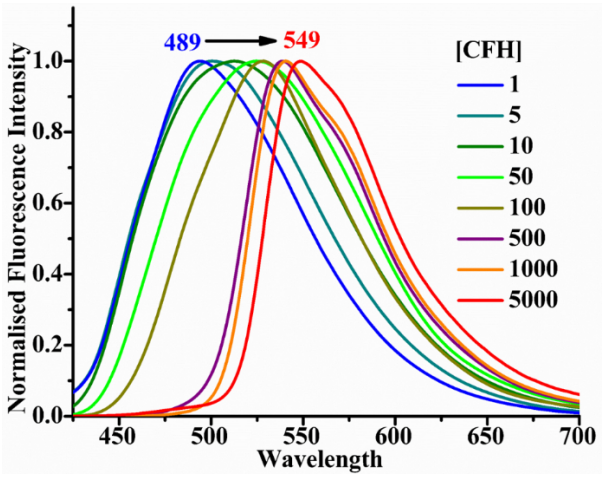

Fig. S13 Normalized fluorescence spectra of **CFH** in THF with increasing concentrations of **CFH** (1 μM-5000 μM). (λ_{ex} = 400 nm, slit = 5 nm)

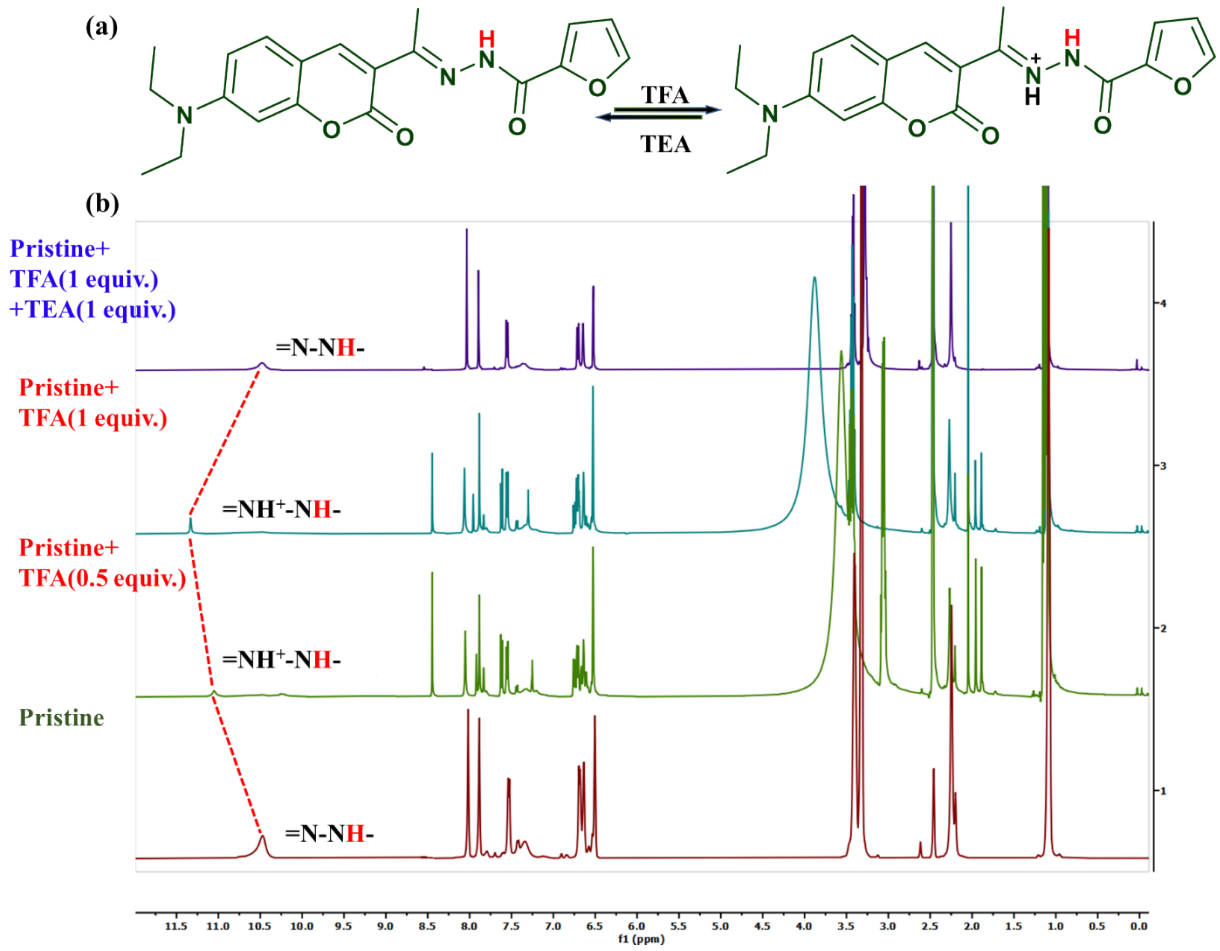

Fig. S14 (a) Schematic representation of protonation of **CFH**. **(b)** ^{1}H NMR titration of **CFH** in DMSO-d_6 on successive incremental addition of TFA/TEA.

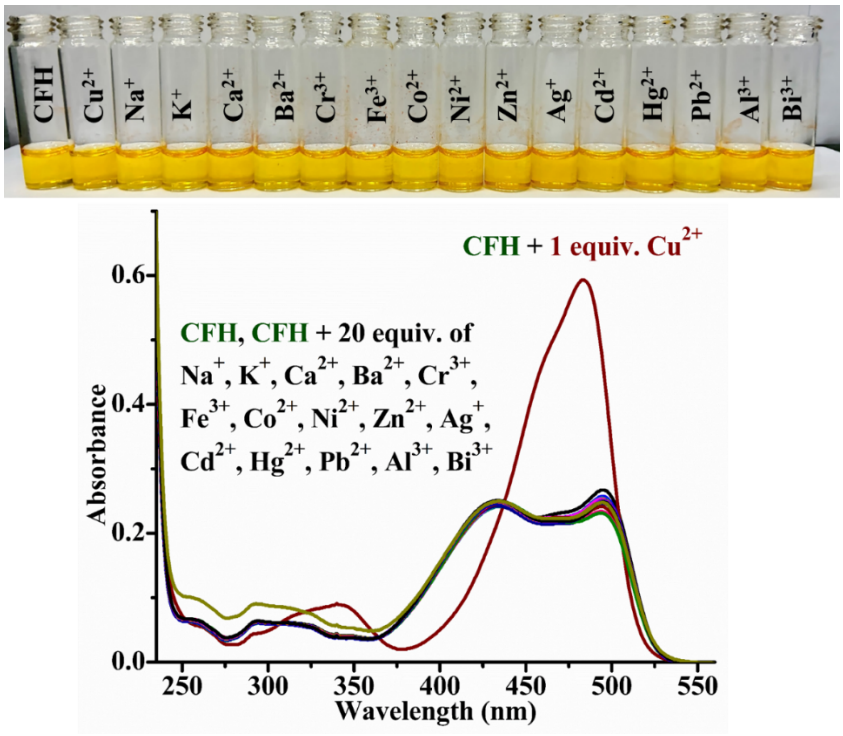

Fig. S15 UV-vis absorption spectra of **CFH** (1 μM) interacting with Cu^{2+} (1 equiv.) and different metal ions (20 equiv.) in water; **(above)** photograph of the **CFH** interacting with metal ions under natural light.

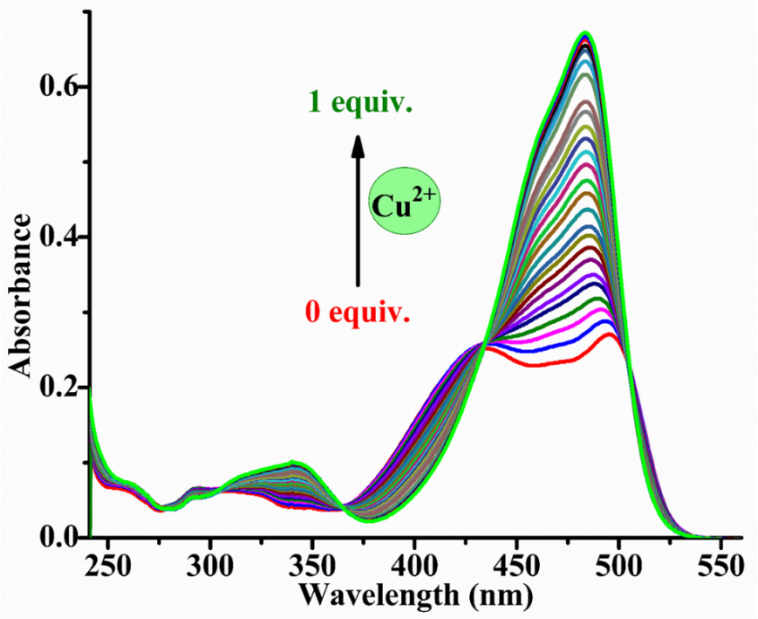

Fig. S16 UV-Vis absorption spectra of **CFH** (1 μM) with different concentrations of Cu^{2+} (0-1 equiv.).

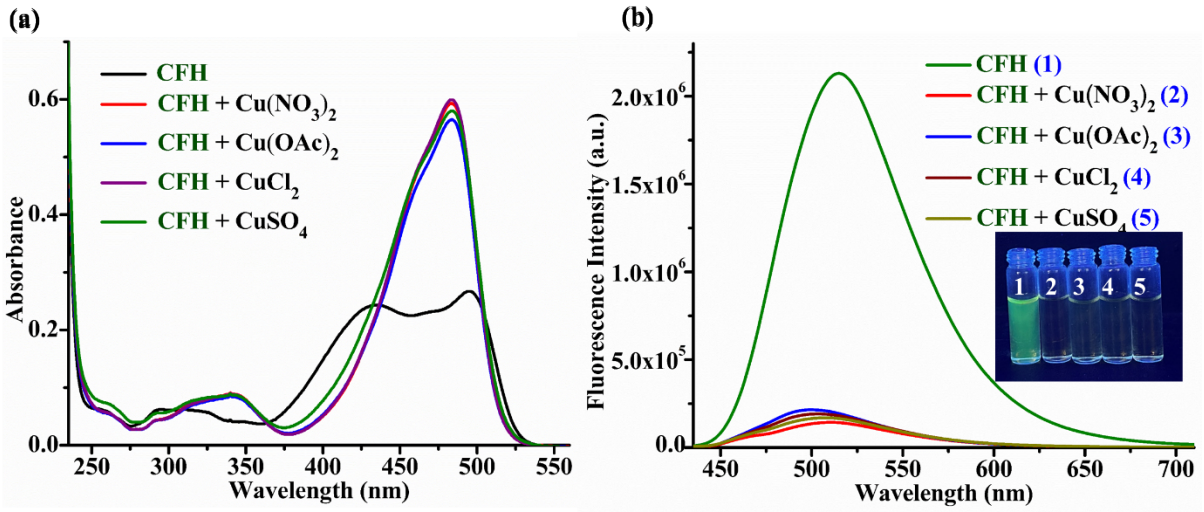

Fig. S17 (a) UV-Vis absorption spectra, **(b)** Fluorescence spectra, of **CFH** (1μM) interacting with different Cu^{2+} salts (1 equiv.) in water**, (inset)** photograph of the **CFH** interacting with different Cu^{2+} salts under 365 nm UV illumination. (λ_{ex} = 400 nm, λ_{em} = 515 nm, slit = 5 nm)

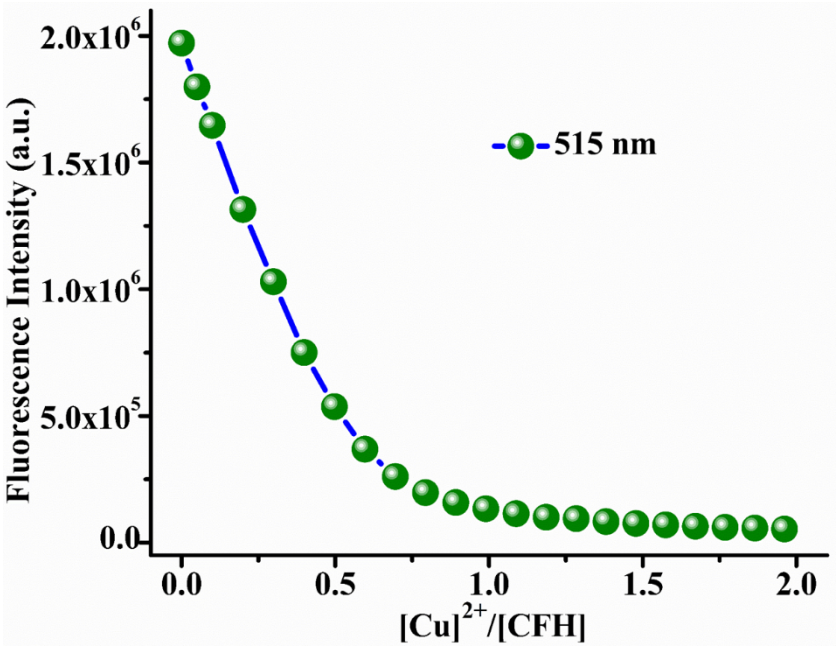

Fig. S18 Fluorescence line graph of $N_{Cu^{2+}}/N_{\mathbf{CFH}}$ system at 515 nm.

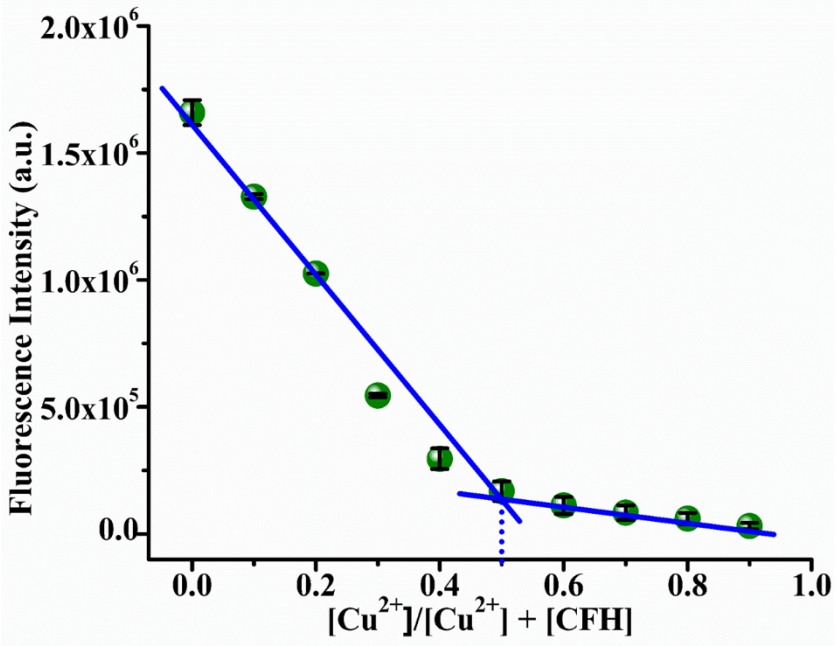

Fig. S19 Job's plot for determination of binding stoichiometry for **CFH**-Cu^{2+}.

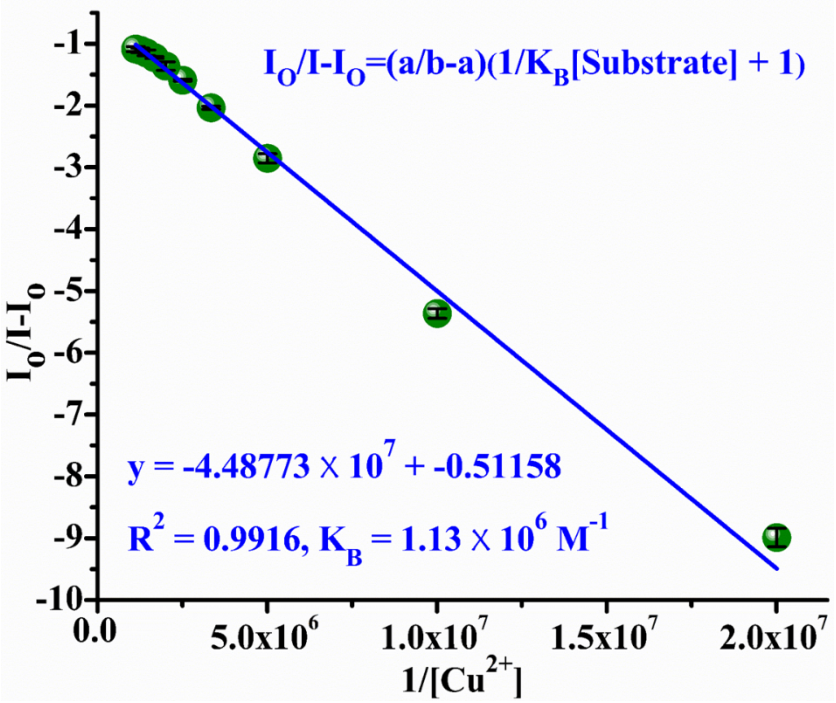

Fig. S20 Benesi-Hildebrand plot of **CFH** for determination of binding constant with Cu^{2+} (R^2 denotes Goodness of fit).

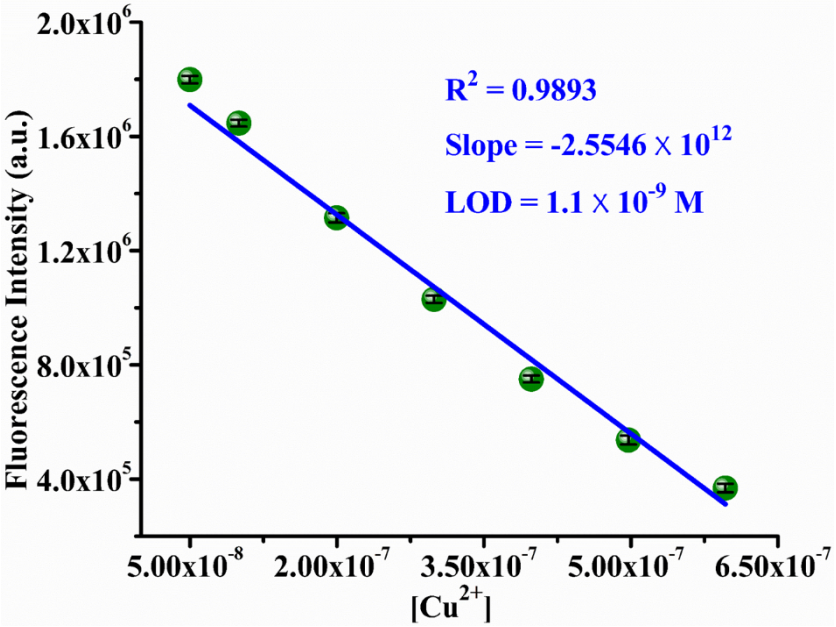

Fig. S21 Limit of detection (LOD = 3σ/Slope) curve plot, the change in fluorescence intensity of **CFH** (1 μM) as a function of Cu^{2+} ions concentration (R^2 denotes Goodness of fit).

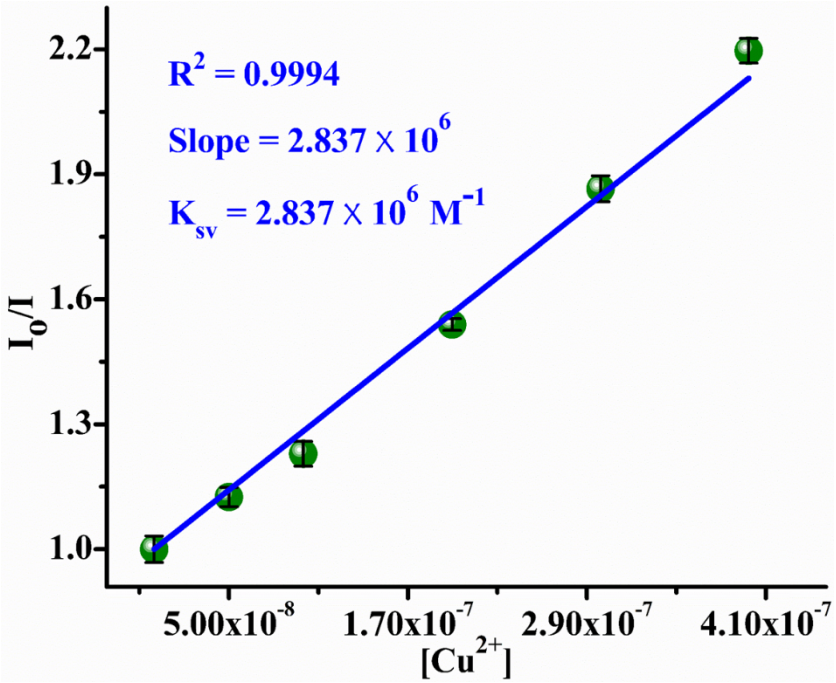

Fig. S22 Stern-Volmer plot for **CFH** in the presence of various concentrations of Cu^{2+}.

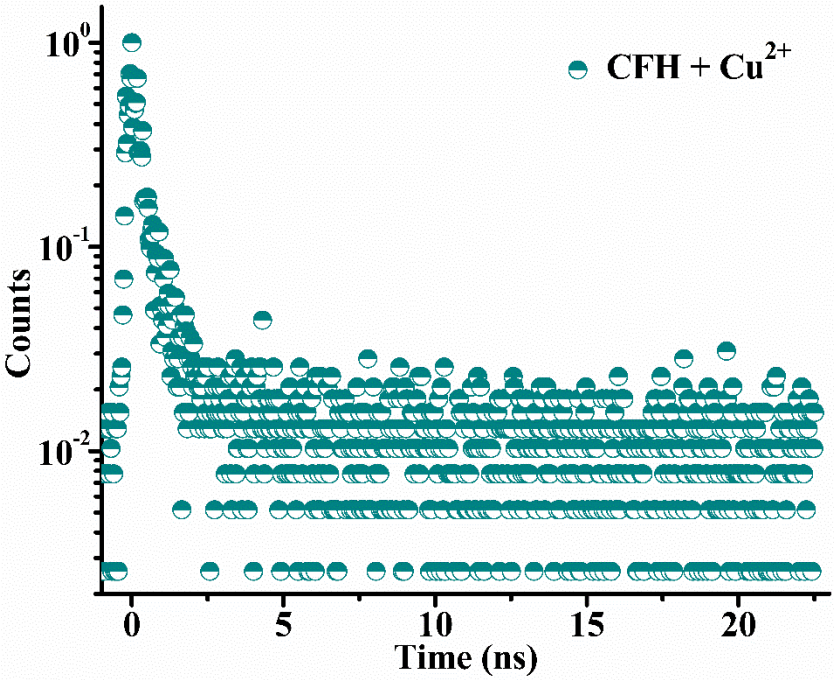

Fig. S23 Time-resolved fluorescence decay profile of **CFH** (1μM) in presence of Cu^{2+} in water.

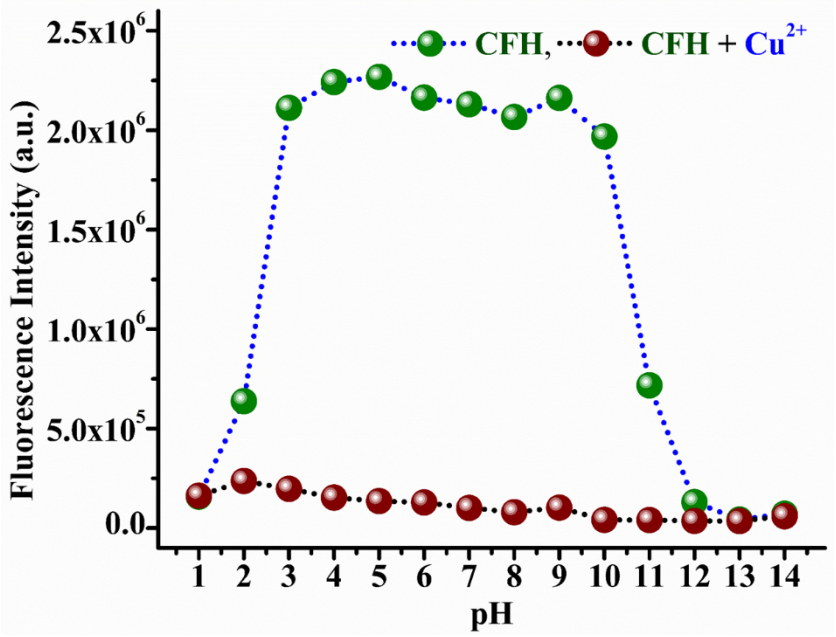

Fig. S24 Effect of pH on the fluorescence intensities of **CFH** (1 μM) at 515 nm in the absence (green spheres) and in the presence (brown spheres) of Cu^{2+} ions (1 equiv.).

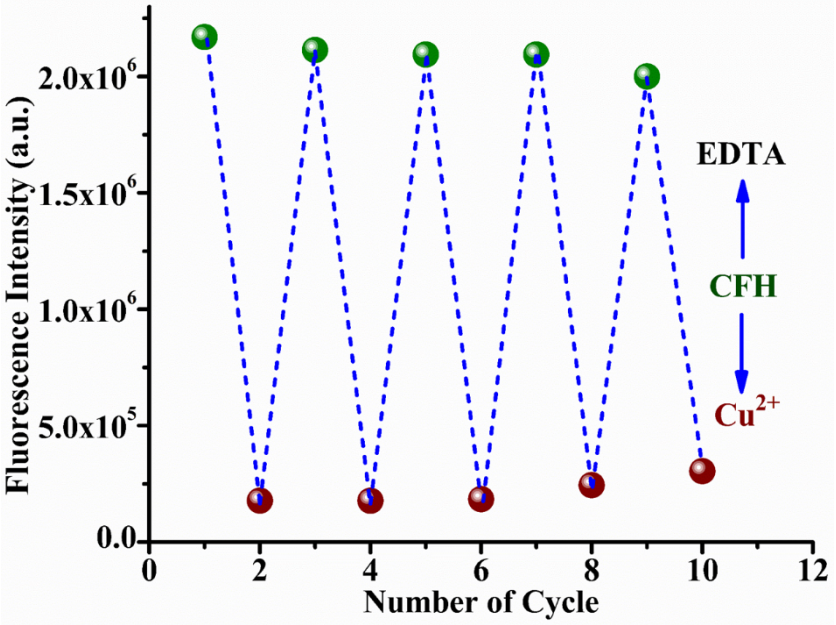

Fig. S25 Fluorescence intensity of **CFH** at 515 nm after the sequential addition of Cu^{2+} and EDTA for five cycles.

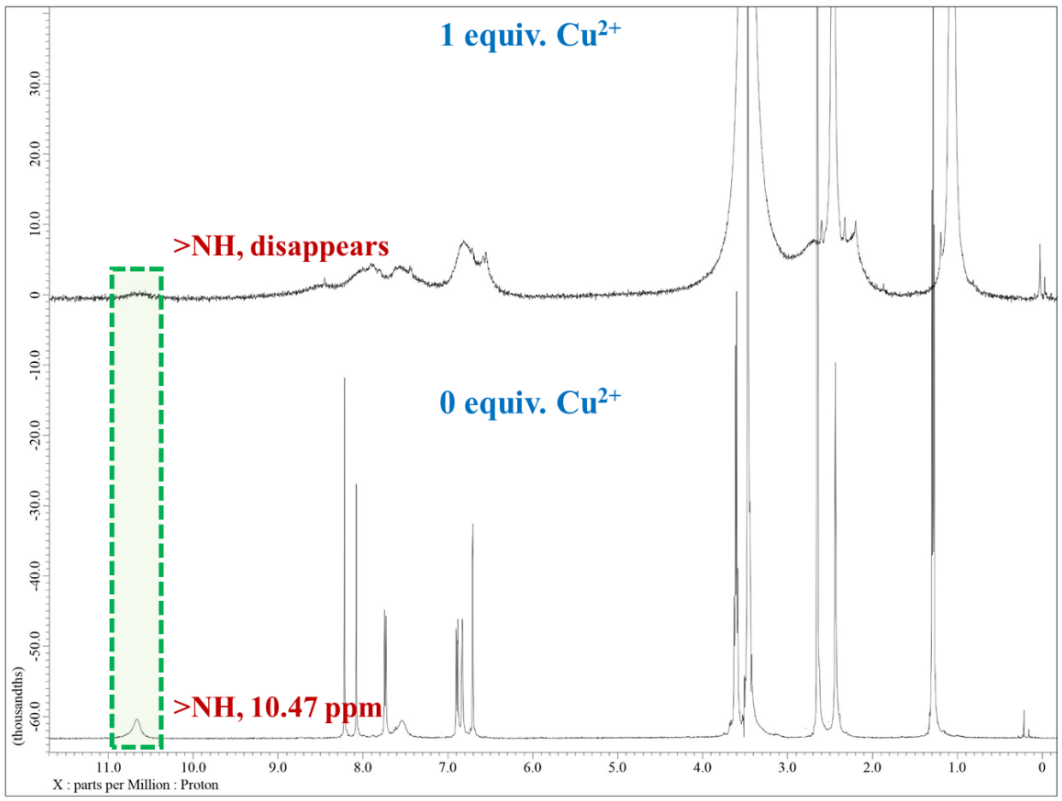

Fig. S26 ^{1}H-NMR titration of **CFH** with Cu^{2+} in DMSO-d_6.

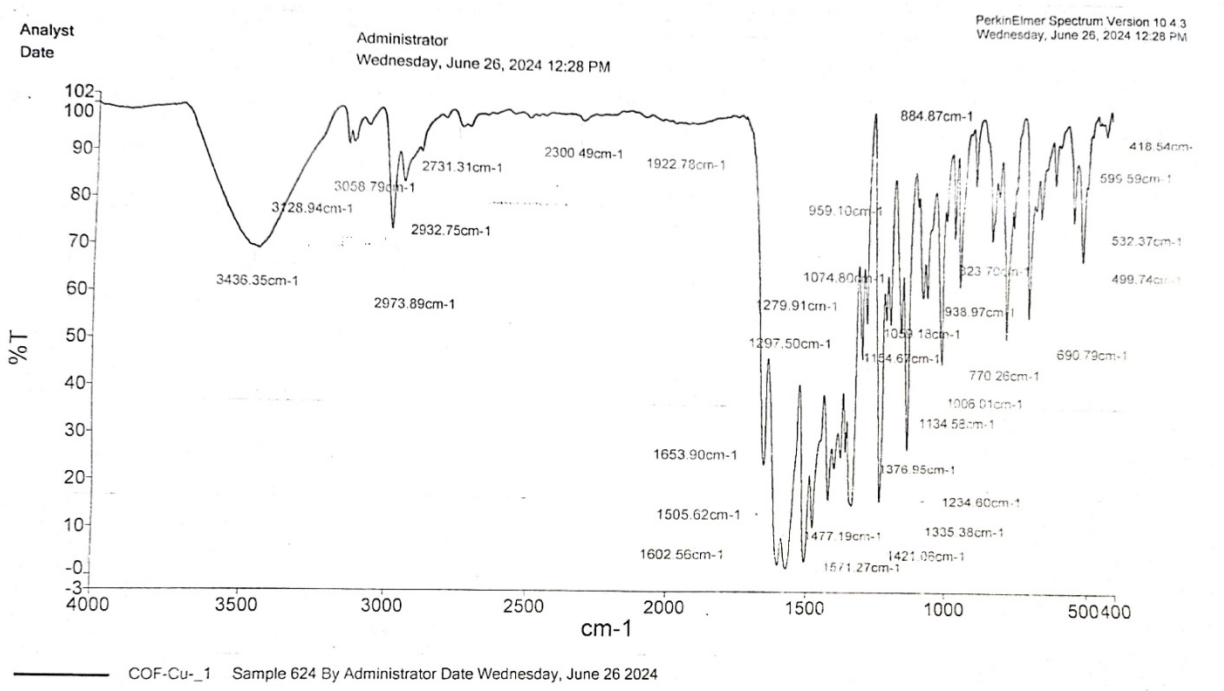

Fig. S27 IR spectrum of **CFH**-Cu^{2+} complex.

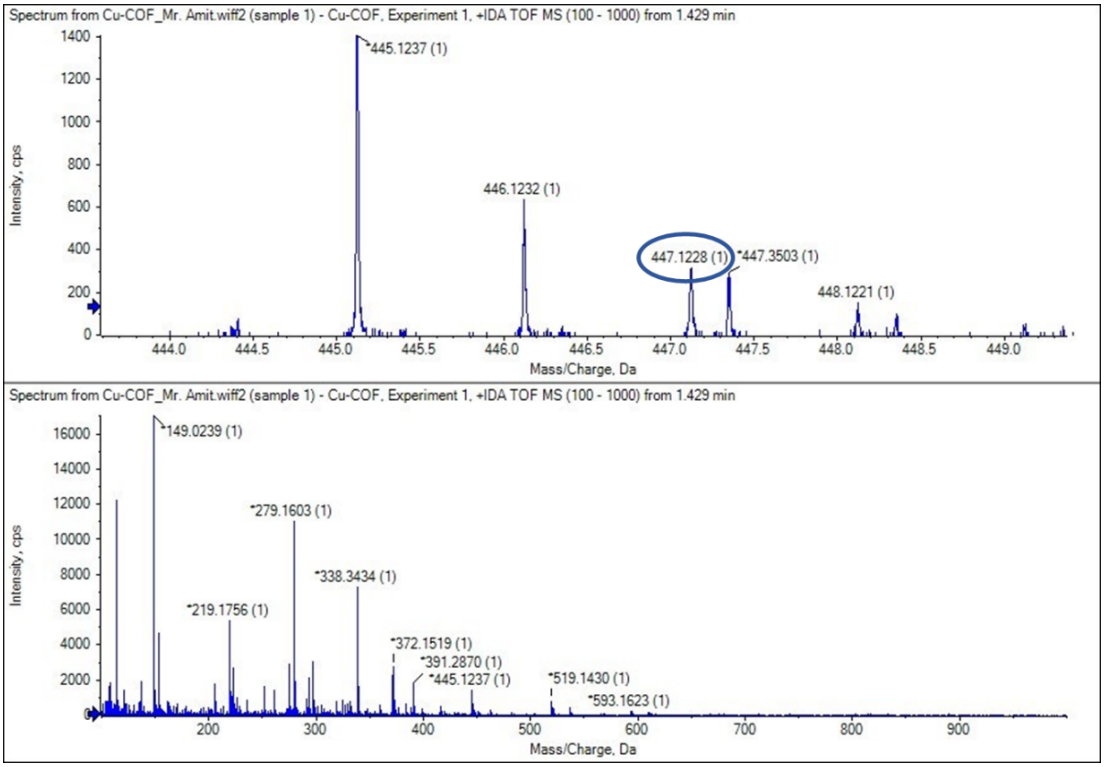

Fig. S28 HRMS spectrum of **CFH**-Cu^{2+} complex.

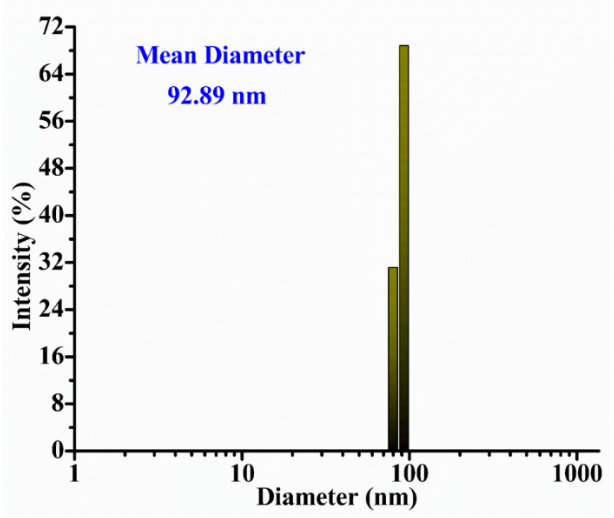

Fig. S29 Particle size measurements by DLS for **CFH** (1μM) in the presence of Cu^{2+} (1 equiv.).

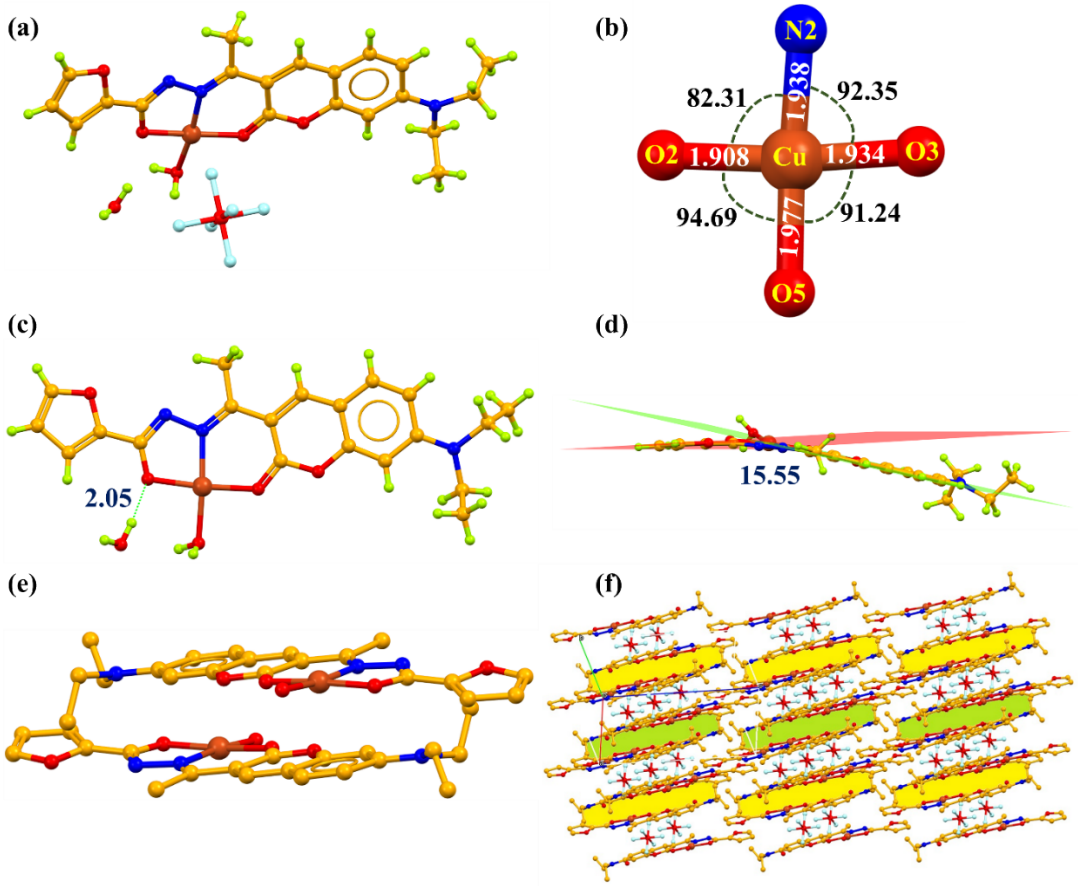

Fig. S30 Molecular packing showing of **CFH**-Cu^{2+}, **(a)** asymmetric unit; **(b)** important bond angles (°) and bond length (Å) around Cu^{2+}; **(c)** inter molecular H-bond (Å) in single crystal lattice of **CFH**-Cu^{2+}; **(d)** angle between the planes of **CFH**-Cu^{2+}; **(e)** head to tail arrangement; **(f)** the molecular packing view along a,b,c-axes.

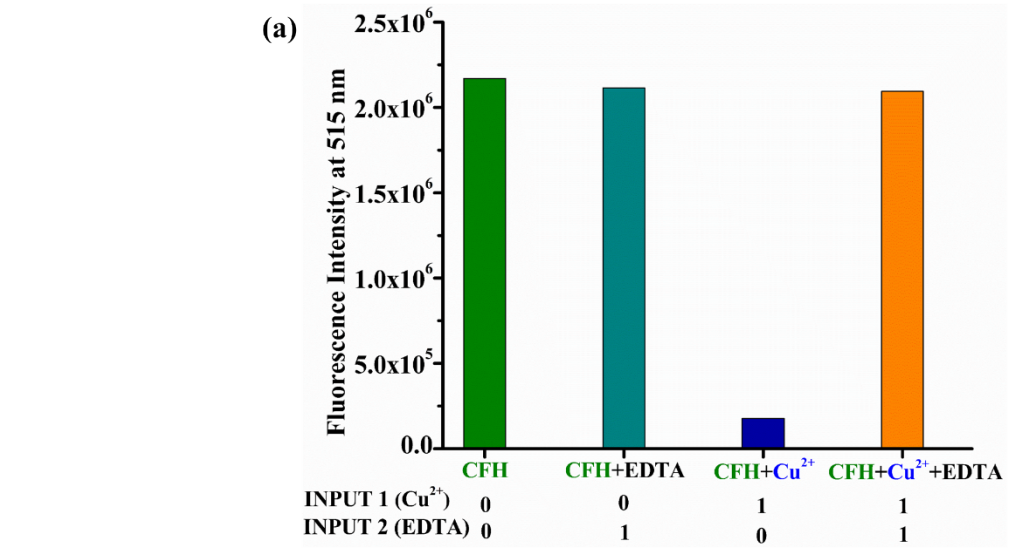

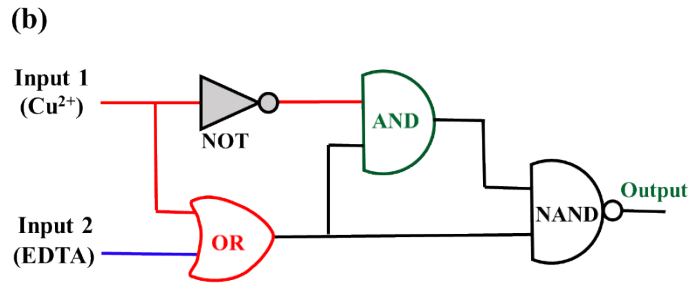

(c)

Input		Output
Input 1 (Cu^{2+})	Input 2 (EDTA)	(Fluorescence Intensity at 515 nm, I_{515})
0	0	1
0	1	1
1	0	0
1	1	1

Fig. S31 (a) Histogram showing emission output at 515 nm. Schematic representation of **(b)** Logic gate and **(c)** Truth table.

Table S1 Crystallographic data for **CFH** and **CFH-**Cu^{2+}.

Parameters	**CFH**	**CFH-**Cu^{2+}
CCDC	**2331258**	**2339921**
Empirical formula	$C_{59.98}H_{62.98}N_{8.99}O_{11.97}$	$C_{20}H_{24}CuF_6N_{2.98}O_6P$
Formula weight	1101.31	610.65
Temperature/K	293	293
Crystal system	monoclinic	triclinic
Space group	$P2_1/c$	P-1
a/Å	14.9321(4)	8.07460(10)
b/Å	13.0338(3)	9.85920(10)
c/Å	30.6182(8)	15.6850(3)
α/°	90	94.4180(10)
β/°	96.843(3)	90.3060(10)
γ/°	90	92.1680(10)
Volume/$Å^3$	5916.5(3)	1244.02(3)
Z	4	2
$\rho_{calc}g/cm^3$	1.236	1.630
μ/mm^{-1}	0.719	2.651
F(000)	2326.0	622.0
Crystal size/mm^3	0.2 × 0.2 × 0.15	0.21 × 0.19 × 0.18
Radiation	Cu Kα (λ = 1.54184)	CuKα (λ = 1.54184)
2Θ range for data collection/°	5.814 to 144.384	5.652 to 144.178
Index ranges	$-18 \le h \le 18$, $-15 \le k \le 16$, $-24 \le l \le 37$	$-7 \le h \le 9$, $-12 \le k \le 12$, $-19 \le l \le 19$
Reflections collected	43142	19689
Independent reflections	11430 [R_{int} = 0.0270, R_{sigma} = 0.0295]	4862 [R_{int} = 0.0861, R_{sigma} = 0.0574]
Data/restraints/parameters	11430/0/772	4862/0/341
Goodness-of-fit on F^2	1.045	1.127
Final R indexes [I>=2σ (I)]	R_1 = 0.0642, wR_2 = 0.1967	R_1 = 0.0797, wR_2 = 0.2305
Final R indexes [all data]	R_1 = 0.0989, wR_2 = 0.2295	R_1 = 0.0857, wR_2 = 0.2392
Largest diff. peak/hole / e $Å^{-3}$	0.41/-0.40	0.99/-1.20

[a] $R_1 = \Sigma||F_o| - |Fc||\Sigma|F_o|$. [b] $R_2 = [\Sigma w(|F^2_o| - |F^2_c|)^2/\Sigma w|F^2_o|^2]^{1/2}$

Table S2 Important bond lengths and bond angles for **CFH.**

Bond Lengths			
Bonds	**Length/Å**	**Bonds**	**Length/Å**
O2-C5	1.237(3)	N2-C7	1.297(3)
N1-C5	1.338(3)	O3-C16	1.221(2)
N2-N1	1.359(3)		
Bond Angles			
Bonds	**Angle/°**	**Bonds**	**Angle/°**
O2-C5-C4	120.3(2)	N2-C7-C8	119.36(19)
O2-C5-N1	125.5(2)	N2-C7-C6	119.4(2)
N1-C5-C4	114.2(2)	O3-C16-C8	126.8(2)
C5-N1-N2	117.49(16)	O3-C16-O4	114.99(19)
C7-N2-N1	124.23(19)		

Table S3 Important bond lengths and bond angles for **CFH-**Cu^{2+}**.**

Bond Lengths			
Bonds	**Length/Å**	**Bonds**	**Length/Å**
O2-C5	1.293(5)	Cu1-O3	1.934(3)
N1-C5	1.303(5)	Cu1-O2	1.908(3)
N2-N1	1.394(4)	Cu1-N2	1.938(3)
N2-C7	1.304(5)	Cu1-O5	1.977(3)
O3-C16	1.245(4)		
Bond Angles			
Bonds	**Angle/°**	**Bonds**	**Angle/°**
O2-C5-C4	116.5(4)	O3-Cu1-N2	92.35(12)
O2-C5-N1	125.2(4)	O3-Cu1-O5	91.24(13)
N1-C5-C4	118.3(4)	O2-Cu1-N2	82.31(12)
C5-N1-N2	117.3(3)	O2-Cu1-O5	94.69(14)
C7-N2-N1	109.5(3)	O2-Cu1-O3	172.64(12)
N2-C7-C8	120.9(3)	N2-Cu1-O5	172.18(14)
N2-C7-C6	121.2(4)	C16-O3-Cu1	126.1(2)
O3-C16-C8	128.1(3)	C5-O2-Cu1	109.9(3)
O3-C16-O4	112.6(3)	N1-N2-Cu1	112.8(2)
		C7-N2-Cu1	129.9(3)

Table S4. Quantum yields and fluorescence decay parameters of **CFH** (1 μM) at different glycerol fraction (f_{gly}) in ethanol.

f_{gly} (%)	A	τ (ns)	<τ> (ns)	ϕ_f (10^{-4})	K_r($^{-}$s) (10^5)	K_{nr}($^{-}$s) (10^9)
50	0.014(A_1) 0.775(A_2)	3.903(τ_1) 0.792(τ_2)	0.85	2.80	3.30	1.17
99.9	0.313(A_1) 0.429(A_2)	0.854(τ_1) 2.349(τ_2)	1.72	14.30	8.31	0.58

Table S5. Quantum yields and fluorescence decay parameters of **CFH** (1 μM) at different water fraction (f_w) in THF and after treatment with Cu^{2+}.

Sample	f_w (%)	A	τ (ns)	<τ> (ns)	ϕ_f (10^{-4})	K_r($^{-}$s) (10^5)	K_{nr}($^{-}$s) (10^9)
CFH	0	0.79(A_1) 0.01(A_2)	0.44(τ_1) 2.17(τ_2)	0.46	2.07	4.50	2.17
CFH	50	0.80(A_1) 0.01(A_2)	0.66(τ_1) 4.02(τ_2)	0.71	5.80	8.18	1.40
CFH	99.9	0.11(A_1) 0.77(A_2)	1.18(τ_1) 0.43(τ_2)	0.52	3.92	7.55	1.92
CFH+Cu^{2+}		0.07(A_1) 0.99(A_2)	1.36(τ_1) 0.28(τ_2)	0.35	0.10	2.87	2.86

Table S6 Comparative account of properties exhibited by **CFH** with other reported probes.

Multi-stimuli responsive behaviour				Biological Application	References
Solid-state		Solution-state			
Properties	**Application**	**Properties**	**Application**		
❖ Mechanochromism (Blue-shifted enhanced emission) ❖ Acidochromism	✓ Defect-sensitive emission ✓ Ultrasound-induced emission ✓ Vapour phase sensing ✓ Anticounterfeiting Application	❖ Solvatochromism ❖ Viscochromism ❖ AIEE ❖ Acidochromism ❖ Metal-ion sensing	✓ Cu^{2+} sensing in pure water ✓ Reversibility with EDTA ✓ Logic gate ✓ Test kit device	✓ Live cell imaging ✓ Neuroprotective therapy for Alzheimer disease	This work
❖ Acidochromism	✓ Vapour phase sensing ✓ Write-Read-Write application	❖ Solvatochromism ❖ AEE ❖ Acidochromism ❖ Metal-ion sensing	✓ Zn^{2+} sensing in ethanol-water (9:1,v/v) ✓ Reversibility with EDTA		11
❖ Mechanochromism (Red-shifted quenched emission) ❖ Photochromism	✓ Rewritable Papers ✓ Photo-Patterning	❖ Solvatochromism ❖ AEE			12
❖ Mechanochromism (Red-shifted quenched emission) ❖ Acidochromism	✓ Vapour phase sensing ✓ Anticounterfeiting Application	❖ Solvatochromism ❖ AIE ❖ Acidochromism			13
❖ Mechanochromism (Red-shifted enhanced emission)		❖ Solvatochromism ❖ AIE ❖ Metal-ion sensing	✓ Al^{3+} sensing in DMF ✓ Reversibility with EDTA		14
❖ Mechanochromism (Blue-shifted enhanced emission) ❖ Acidochromism	✓ Mono and Multi-level decryption	❖ Solvatochromism ❖ Viscochromism ❖ AIE ❖ Acidochromism			15
❖ Mechanochromism (Red-shifted quenched emission)	✓ Rewritable papers	❖ Viscochromism ❖ AIE ❖ Metal-ion sensing	✓ Zn^{2+}/Cu^{2+} sensing in DMF-water (3:7, pH 7.4) HEPES buffer solution ✓ Reversibility with EDTA ✓ Logic gate ✓ Test kit	✓ Live cell imaging	16
❖ Mechanochromism (Red-shifted ❖ quenched emission)		❖ Solvatochromism ❖ AIE ❖ Metal-ion sensing	✓ Cu^{2+} sensing in THF		17
❖ Mechanochromism (Blue-shifted quenched emission)		❖ Solvatochromism ❖ AIE ❖ Analyte sensing	✓ Nitroexplosive sensing in 40:60 (THF: H_2O) ✓ Test strips		18

References

1. O. V. Dolomanov, L. J. Bourhis, R. J. Gildea, J. A. K. Howard and H. Puschmann, OLEX2: a complete structure solution, refinement and analysis program, *J. Appl. Crystallogr.*, 2009, **42**, 339-341.
2. G. M. Sheldrick, *Acta Crystallogr., Sect. A. Struct. Chem.,* 2015, **71**, 3-8.
3. L. J. Farrugia, WinGX suite for small-molecule single-crystal crystallography. *J. Appl. Crystallogr.,* 1999, **32**, 837-838.
4. J. Luo, Z. Xie, Z. Xie, J. W. Y. Lam, L. Cheng, H. Chen, C. Qiu, H. S. Kwok, X. Zhan, Y. Liu, D. Zhu and B. Z. Tang, Aggregation-induced emission of 1-methyl-1, 2, 3, 4, 5-pentaphenylsilole, *Chem. Commun.*, 2001, **18**, 1740-1741.
5. K. R. Barqawi, Z. Murtaza and T. J. Meyer, Calculation of relative nonradiative decay rate constants from emission spectral profiles: polypyridyl complexes of ruthenium(II), J. *Phys. Chem.*, 1991, **95**, 47–50.
6. H. A. Benesi and J. H. Hildebrand, A spectrophotometric investigation of the interaction of iodine with aromatic hydrocarbons, *J. Am. Chem. Soc.*, 1949, **71**, 2703-2707.
7. G. L. Long and J. D. Winefordner, Principles of environmental analysis, *Am. Chem. Soc.*, 1983, **55**, 712A-724A.
8. J. R. Lakowicz, Principles of fluorescence spectroscopy, University of Maryland, School of Medicine, Baltimore*,* 2006, **132.**
9. D. Jacquemin, B. Mennucci, and C. Adamo. Excited-state calculations with TD-DFT: from benchmarks to simulations in complex environments, *Physical chemistry chemical physics*, 2011, **13**, 16987-16998.
10. G. A. Petersson and A.-L. Mohammad A., A complete basis set model chemistry. II. Open-shell systems and the total energies of the first-row atoms, *J. Chem. Phys.*, 1991, **9**, 6081-6090.
11. P. Pallavi, V. Kumar, M. W. Hussain and A. Patra, Excited-State Intramolecular Proton Transfer-Based Multifunctional Solid-State Emitter: A Fluorescent Platform with "Write-Erase-Write" Function, *ACS Appl. Mater. Interfaces,* 2018*,* **10***,* 44696-44705.
12. W. Luo, Y. Tang, X. Zhang, Z. Wu and G. Wang, Multifunctional Fluorescent Materials with Reversible Mechanochromism and Distinct Photochromism, *Adv. Optical Mater.*, 2023, **11**, 2202259.

13. O. Anitha, M. Mathivanan, B. Tharmalingam, T. Thiruppathiraja, S. Ghorai, R. Natarajan, V. Thiagarajan, S. Lakshmipathi and B. Murugesapandian, Multi-stimuli responsiveness of pyrimidine bishydrazone: AIE, tuneable luminescence, white light emission, mechanochromism, acidochromism and its anticounterfeiting applications, *Dyes and Pigments,* 2023, **212**, 111091.
14. K. Santhiya, S. K. Sen, R. Natarajan, R. Shankar and B. Murugesapandian, D–A–D Structured Bis-acylhydrazone Exhibiting Aggregation-Induced Emission, Mechanochromic Luminescence, and Al(III) Detection, *J. Org. Chem.,* 2018, **83**, 10770-10775.
15. W. Zhong, J. Zhang, Y. Lin, S. Li, Y. Yang, W. J. Wang, C. Si, F. E. Kühn, Z. Zhao X. M. Cai and B. Z. Tang, Multi-site isomerization of synergistically regulated stimuli-responsive AIE materials toward multi-level decryption, *Chem. Sci.,* 2024, **15**, 3920-3927.
16. A. Singh, P. Yadav, S. Singh, P. Kumar, S. Srikrishna and V. P. Singh, A multifunctional coumarin-based probe for distinguishable detection of Cu^{2+} and Zn^{2+}: its piezochromic, viscochromic and AIE behavior with real sample analysis and bio-imaging applications, *J. Mater. Chem. C*, 2023, **11**, 13056-13066.
17. L. Shen, C. J. Yu, H. F. Xie, N. Xu, H. Xu, Y. L. Huang, C. Redshaw, X. Feng and Q. L. Zhang, Naphthaldehyde-based Schiff base dyes: aggregation-induced emission and high-contrast reversible mechanochromic luminescence, *Mater. Chem. Front.*, 2022, **6**, 2491-2498.
18. K. Duraimurugan, M. Harikrishnan, J. Madhavan, A. Siva, S. J. Lee, J. Theerthagiri and M. Y. Choi, Anthracene-based fluorescent probe: Synthesis, characterization, aggregation-induced emission, mechanochromism, and sensing of nitroaromatics in aqueous media, *Environmental Research*, 2021, **194***,* 110741.

.